

Fine Structures of Shock of SN 1006 with the *Chandra* Observation

Aya Bamba, Ryo Yamazaki, Masaru Ueno, and Katsuji Koyama

*Department of Physics, Graduate School of Science, Kyoto University, Sakyo-ku, Kyoto
606-8502, Japan*

bamba@cr.scphys.kyoto-u.ac.jp, yamazaki@tap.scphys.kyoto-u.ac.jp,
masaru@cr.scphys.kyoto-u.ac.jp, koyama@cr.scphys.kyoto-u.ac.jp

ABSTRACT

The north east shell of SN 1006 is the most probable acceleration site of high energy electrons (up to ~ 100 TeV) with the Fermi acceleration mechanism at the shock front. We resolved non-thermal filaments from thermal emission in the shell with the excellent spatial resolution of *Chandra*. The thermal component is extended widely over about ~ 100 arcsec (about 1 pc at 1.8 kpc distance) in width, consistent with the shock width derived from the Sedov solution. The spectrum is fitted with a thin thermal plasma of $kT = 0.24$ keV in non-equilibrium ionization (NEI), typical for a young SNR. The non-thermal filaments are likely thin sheets with the scale widths of ~ 4 arcsec (0.04 pc) and ~ 20 arcsec (0.2 pc) at upstream and downstream, respectively. The spectra of the filaments are fitted with a power-law function of index 2.1–2.3, with no significant variation from position to position. In a standard diffusive shock acceleration (DSA) model, the extremely small scale length in upstream requires the magnetic field nearly perpendicular to the shock normal. The injection efficiency (η) from thermal to non-thermal electrons around the shock front is estimated to be $\sim 1 \times 10^{-3}$ under the assumption that the magnetic field in upstream is $10 \mu\text{G}$. In the filaments, the energy densities of the magnetic field and non-thermal electrons are similar to each other, and both are slightly smaller than that of thermal electrons. In the same order for each other. These results suggest that the acceleration occur in more compact region with larger efficiency than previous studies.

Subject headings: acceleration of particles — supernova remnants: individual (SN 1006) — X-rays: ISM

1. Introduction

Since the discovery of cosmic rays (Hess 1912), the origin and acceleration mechanism up to $10^{15.5}$ eV (the “knee” energy) have been long-standing problems. A breakthrough came

from the X-ray studies of SN 1006; Koyama et al. (1995) discovered synchrotron X-rays from the shells of this SNR, indicating the existence of extremely high energy electrons up to the knee energy produced by the first order Fermi acceleration. Further, Tanimori et al. (1998) confirmed the presence of high energy electrons with the detection of the TeV γ -rays, which are cosmic microwave photons up-scattered by high energy electrons (the inverse Compton process) in the north east shell (the NE shell) of SN 1006. The combined analysis of the synchrotron X-rays and inverse Compton TeV γ -rays nicely reproduces the observed flux and spectra, and predicts a rather weak magnetic field of 4–6 μ G (Tanimori et al. 1998, 2001).

Since these discoveries, detection of synchrotron X-rays and/or TeV γ -rays, from other shell-like SNRs has been accumulating: G347.3–0.5 (Koyama et al. 1997; Slane et al. 1999; Muraishi et al. 2000; Enomoto et al. 2002), RCW 86 (Bamba et al. 2000; Borkowski et al. 2001b), and G266.6–1.2 (Slane et al. 2001). These discoveries provide good evidence for the cosmic ray acceleration at the shocked shell of SNRs. The mechanism of the cosmic ray acceleration has also been studied for a long time and the most plausible process is a diffusive shock acceleration (DSA) (Bell 1978; Blandford & Ostriker 1978; Drury 1983; Blandford & Eichler 1987; Jones & Ellison 1991; Malkov & Drury 2001).

Apart from the globally successful picture of DSA, detailed but important processes, such as the injection, magnetic field configuration, and the reflection of accelerated particles, have not yet been well understood. The spatial distribution of accelerated particles responsible for the non-thermal X-rays, may provide key information on these unclear subjects. Previous observations, however, are limited in spatial resolution for a detailed study on the structure of shock acceleration process and injection efficiency. Although many observations and theoretical models are made for SN 1006, these problems are still open issue (Reynolds 1998; Aharonian & Atoyan 1999; Vink et al. 2000; Ellison, Berezhko, & Baring 2000; Dyer et al. 2001; Allen, Petre, & Gotthelf 2001; Berezhko et al. 2002).

In this paper, we report on the first results of the spectral and spatial studies on the thermal and non-thermal shock structure in the NE shell of SN 1006 with *Chandra* (§ 3). In § 4.1 and § 4.2, we discuss the spectral analyses and determine the scale widths of the structures for thermal and non-thermal electrons on the base of a simple DSA with shock parallel magnetic field. We also derive the injection efficiency (η) of non-thermal electrons from the thermal plasma near the shock front. Based on these results, we discuss possible implications on the DSA process in the NE shell of SN 1006. In this paper, we assume the distance of SN 1006 to be 1.8 kpc (Green 2001).

2. Observation

We used the *Chandra* archival data of the ACIS on the NE shell of SN 1006 (Observation ID = 00732) observed on July 10–11, 2000 with the targeted position at (RA, DEC) = ($15^{\text{h}}03^{\text{m}}51^{\text{s}}.6$, $-41^{\text{d}}51^{\text{m}}18^{\text{s}}.8$). The satellite and instrument are described by Weisskopf et al. (1996) and Garmire et al. (2000), respectively. CCD chips I2, I3, S1, S2, S3, and S4 were used with the pointing center on S3. Data acquisition from the ACIS was made in the Timed-Exposure Faint mode with the readout time of 3.24 s. The data reductions and analyses were made using the *Chandra* Interactive Analysis of Observations (CIAO) software version 2.2.1. Using the Level 2 processed events provided by the pipeline processing at the *Chandra* X-ray Center, we selected *ASCA* grades 0, 2, 3, 4, and 6, as the X-ray events. High energy electrons due to charged particles and hot and flickering pixels were removed. The effective exposure was ~ 68 ks for the observation. In this paper, we concentrated on the data of S3 (BI chip) because this chip has the best efficiency in soft X-rays required for the spectral analyses and its on-axis position provides the best point-spread function required for the spatial analysis.

3. Analyses and Results

3.1. Overall Image

Figure 1 shows the true-color image from I2, I3, and S1–S4 for the NE shell of SN 1006. The image is contrasted in the 0.5–2.0 keV band (hereinafter, the soft1 band; red) and in the 2.0–10.0 keV band (hereinafter, the hard band; blue) and binned to a resolution of 1 arcsec. The fine spatial resolution of *Chandra* unveils extremely narrow filaments in the hard band. They are running from north to south along the outer edge of the NE shell, parallel to the shock fronts observed by $\text{H}\alpha$ emission line (Winkler & Long 1997). These filaments resemble the sheet-like structure of the shock simulated by Hester (1987). The soft1 band image, on the other hand, has a larger scale width similar to the *ROSAT* HRI image (Winkler & Long 1997). Many clumpy sub-structures are also seen in this energy band.

3.2. Inner Shell Region

To resolve the thermal and non-thermal components, we made a spectrum from a bright clump found in the soft1 band image, which is located in the inner part of the NE shell (“Inner region” with the dashed ellipse in Figure 2). The background region was selected from a

region out of the SNR, as is shown in Figure 2 with the dashed lines.

The background-subtracted spectrum shown in Figure 3 has many emission lines. We hence determined the peak energies of the 5 brightest lines with a phenomenological model, a power-law continuum plus Gaussian lines. The most strong line structures are the peak at 0.55 keV and the hump at 0.67 keV. These energies are nearly equal to the $K\alpha$ and Lyman α lines of He- and H-like oxygen, hence are attributable to highly ionized oxygen. Likewise, the other clear peaks at 0.87, 1.31, and 1.76 keV are most likely He-like $K\alpha$ of Ne, Mg and Si, respectively. However, in detail all the observed line energies are systematically smaller than those of the relevant atomic data. These apparent energy shifts have been usually observed in a young SNR plasma in non-equilibrium ionization (NEI). The “energy shift” in this case is due to the different line ratio of many sub-levels and/or different ionization states. The oxygen Lyman α is isolated from the other lines of different ionization states, hence the NEI effect gives no energy shift. Still we see apparent down-shift of the observed line energy from that of the laboratory data. He-like $K\alpha$ lines are complex of many fine structures with the split-energy of at most ~ 25 eV (for He-like silicon). Although the energy shift of He-like $K\alpha$ lines due to NEI should be smaller than this split-energy, the observed energy shifts are systematically larger than the split-energy. We therefore regard that the apparent energy shifts are due mainly to energy calibration errors, hence fine-tuned the energy gain to reduce by 3.8%, the average shift of the 5 brightest lines. We then fitted the spectrum with a thin thermal plasma model in NEI calculated by Borkowski et al. (2001a). The abundances of C, N, O, Ne, Mg, Si, S, and Fe in the plasma were treated to be free parameters, whereas those of the other elements were fixed to the solar values (Anders & Grevesse 1989). The absorption column was calculated using the cross sections by Morrison & McCammon (1983) with the solar abundances. Since this NEI model exhibited systematic data excess at high energy above 2 keV, we added a power-law component and the fit improved dramatically. Figure 3 and Table 1 show the best-fit models (dashed and solid lines for thermal and power-law components) and parameters, respectively.

Instead of the phenomenological power-law model, we applied *srcut* in the XSPEC package as a more physical model. Details of the *srcut* model fitting are given in § A.1. The best-fit ν_{rolloff} is $9.2 (8.6\text{--}10.3) \times 10^{16}$ Hz, with better reduced χ^2 of 389.0/215 than that of the power-law model of 447.9/215 (see Table 1).

As for the thermal components, we also tried the fitting with a plane shock model (XSPEC model *vpshock*) plus either a power-law or *srcut* and found no essential difference from the case of an NEI model.

Although these simple models globally follow the data very well, all are rejected in the statistical point of view, leaving wavy residuals near the line structure as shown in Figure 3

(lower panel). This may be caused by improper response function in energy scale and/or in energy resolution. We assumed that the photons are uniformly distributed in flux and in temperature through the whole source region. This simple assumption may also partly responsible for the above systematic error, because in reality the source region is apparently clumpy (see Figure 1) and may have different temperatures, abundances, and/or ionization time scales. Since our principal aim of this paper is to examine the spatial structures and the spectra of non-thermal component, we do not examine in further detail for the thermal model. In the following analyses and discussion, we use the physical parameters cited in Table 1 as a good approximation.

The spectrum of the inner region clump is softer than any other regions in the NE shell, which indicates that the contribution of the thermal component is the largest. Nevertheless the thermal photons are only 0.02% of the non-thermal ones if we limit the energy band to 2.0–10.0 keV (the hard band); the non-thermal photons in the hard band are 8.9×10^{-2} cts s⁻¹, while thermal photons are 2.0×10^{-5} cts s⁻¹. Therefore, in the following spatial analyses, we regard that all the photons in the hard band are non-thermal origin.

As for the spatial analysis of the thermal emission, we use the limited band of 0.4–0.8 keV (hereafter; the soft2 band) to optimize the signal-to-noise ratio, in which K-shell lines from He-like oxygen (0.57 keV) contribute a most fraction of the X-ray emission (see Figure 3). Even in this thermal-optimized band, however, the count rates of the thermal and non-thermal emissions are comparable: thermal photons are 8.1×10^{-1} cts s⁻¹, while those of non-thermal are 5.4×10^{-1} cts s⁻¹.

3.3. The Filaments

The outer edge of the NE shell is outlined by several thin X-ray filaments. For the study of these filaments, we selected 6 rectangle regions in Figure 1, in which the filaments are straight and free from other structures like another filament and/or clumps. These regions (solid boxes) are shown in Figure 2 with the designations of No.1–6 from north to south. Since the SNR shell is moving (expanding) from the right to the left, we call the right and left side as downstream and upstream following the terminology of the shock phenomena.

Figure 4 shows the intensity profile in the hard (2.0–10.0 keV: upper panel) and soft2 (0.4–0.8 keV: lower panel) bands for each filament with the spatial resolution of 0.5 arcsec, where the horizontal axis (x -coordinate) runs from the east to west (upstream to downstream) along the line normal to the filaments. We see very fast decay in the downstream side and even faster rise in the upstream side.

To estimate the scale width, we define a simple empirical model as a function of position (x) for the profiles;

$$f(x) = \begin{cases} A \exp \left| \frac{x_0 - x}{w_u} \right| & \text{in upstream} \\ A \exp \left| \frac{x_0 - x}{w_d} \right| & \text{in downstream,} \end{cases} \quad (1)$$

where A and x_0 are the flux and position at the filament peak, respectively. The scale widths are given by w_u and w_d for upstream and downstream, respectively (hereafter, “u” and “d” represent upstream and downstream, respectively). Since the scale width of the filaments is larger than the spatial resolution of *Chandra* (~ 0.5 arcsec = 1 bin in Figure 4), we ignore the effect of the point-spread function.

3.3.1. Non-Thermal Structure

As already noted in § 3.2, the hard band (2.0–10.0 keV) flux is nearly pure non-thermal origin (see also the next paragraph). We therefore used the hard band profiles for the study of the non-thermal X-ray structures. The hard band profiles were fitted with a function $f^h(x) + C^h$ (hereafter, “h” represents the hard X-ray band), where C^h is the background constant, which includes the cosmic and Galactic X-ray background and non X-ray events. The fittings were statistically accepted for all the filament profiles. The best-fit models and parameters are shown in Figure 4 with the solid lines and in Table 2, respectively.

We then made the spectra of the filaments within the scale widths: ($x_0^h - w_u^h \leq x \leq x_0^h + w_d^h$) in Figure 4. The background spectra were made from the off-filament downstream regions. All the background-subtracted spectra are featureless (no line structure) and extend to high energy side, which were fitted with an absorbed power-law model with the best-fit parameters given in Table 3. We thus confirm that the hard X-ray profiles represent those of non-thermal X-rays.

To increase statistics, we summed all the data of 6 filaments (the combined-filament). The best-fit power-law model parameters for the spectrum of the combined-filament are listed in Table 3. The spectrum was also fitted with a *srcut* model (see § A.1). The best-fit ν_{rolloff} and the other parameters are also listed in Table 3. We note that the *srcut* model give slightly better $\chi^2/\text{d.o.f.}$ than that of a phenomenological power-law model (see Table 3).

We further spatially divided the combined-filament and analyzed each spectrum. We however found no significant difference between the downstream and upstream, nor within the downstream; the photon index was nearly constant along the x -axis in the combined-filament.

3.3.2. Thermal Structure

To examine the structure of the thermal components, we used the soft2 band profiles (the lower panels of Figure 4). Contamination from the non-thermal photons would be very large even in this optimized band (see § 3.2). Therefore we calculated the flux ratio of the non-thermal photons between in the hard and soft2 bands using the spectral parameters given in Table 3. From the flux ratio and the best-fit hard band profiles, we estimated the non-thermal contaminations as are given with the dashed lines in Figure 4.

After subtracting these non-thermal contaminations, we fitted the soft2 band profiles with a model of $f^s(x) + C^s$, where C^s is the background constant in the same sense as C^h . Note that although we use “s” as the abbreviation of the soft2 band, it actually represents thermal X-rays.

From Figure 4, we see that most of the photons at the filament peak is non-thermal origin, hence the statistics becomes poor to determine the position of the thermal peak (x_0^s) independently. We thus fixed x_0^s to the best fit peak in the hard band x_0^h . Also we set the upper bound of the fitting parameter w_d^s to be 900 arcsec, the same as the radius of SN 1006 (Green 2001). The best-fit models and parameters for the thermal components ($f^s(x)$) are shown with dotted lines in the lower panels of Figure 4 and in Table 2, respectively.

3.3.3. Non-Thermal versus Thermal

Figure 5(a) shows the relation of the scale widths between the downstream and upstream sides for each filament. Although there is a large scatter, w_u is systematically smaller than w_d in both the non-thermal and thermal emissions.

Figure 5(b) shows the relation between w^s and w^h . We find that w_d^s is significantly larger than w_d^h , whereas w_u^s and w_u^h are comparable with each other. The mean values are $\overline{w_u^s} = 4.3$ arcsec = 0.04 pc, $\overline{w_d^s} = 1.3 \times 10^2$ arcsec = 1.1 pc, $\overline{w_u^h} = 5.1$ arcsec = 0.04 pc, and $\overline{w_d^h} = 18$ arcsec = 0.2 pc. Note that the minimum value of w_u^h is only 0.98 arcsec = 0.01 pc (filament 4). Maybe since their wide scatter is due to that these are the projected values of the possible sheet-like with wavy and/or curved shape.

4. Discussion

4.1. Thermal Plasma

Although the best-fit NEI model in Table 1 is rejected statistically, it globally fits the thermal emission of SN 1006 as shown in Figure 3. The temperature ($kT=0.24$ keV) is similar to the results obtained by Vink et al. (2000), Dyer et al. (2001), and Allen, Petre, & Gotthelf (2001), but lower than that by Koyama et al. (1995). Since the spatial resolution of *Chandra* enables us to remove the non-thermal photons from the thermal emission more accurately than the *ASCA* case, the present results should give a more precise description on the thermal plasma. Like the previous observations (Koyama et al. 1995; Allen, Petre, & Gotthelf 2001), heavy elements, in particular iron, are overabundant, which implies that the X-ray emitting thermal plasma is dominated by the ejecta from type Ia SN. The fact that the thermal emission is enhanced at the inner shell region also suggests the ejecta origin.

From the emission measure (EM) and assuming a uniform density plasma of a prolate shape with the 3-axis radii of 140, 120, and 120 arcsec, we estimate the density n_e in the inner region to be 0.36 cm^{-3} . Then from the best-fit ionization parameter, τ is $2.6 \times 10^{10} \text{ s} = 8.3 \times 10^2 \text{ yr}$, roughly consistent with the age of SN 1006.

Even in the soft2 band profiles, the thermal components are not prominent (see Figure 4), which prevents us from high quality study for the morphology of the thermal plasma. Nevertheless, we found that the profiles of thermal filaments are largely anti-symmetric. The scale width w_u^s is very sharp and comparable to w_u^h , whereas w_d^s shows a relatively large scale width. Although w_u^s couples to x_0 , which is frozen to the best-fit value in the hard band (see Figure 5(b)), we can say that the thermal shock has very sharp rise in upstream.

The downstream scale width w_d^s is comparable to the shock width derived from the Sedov solution of about $75 \text{ arcsec} = 0.7 \text{ pc}$ for SN 1006 having a $15 \text{ arcmin} = 8 \text{ pc}$ radius (Green 2001). Therefore, the thermal filaments may nicely trace the density profiles of the Sedov solution.

4.2. Non-Thermal Filaments

In this section, we interpret the scale width of hard band X-rays in upstream, w_u^h .

The hardest spectral regions, the non-thermal filaments, are the most probable site of the maximum energy acceleration. From the observation alone, we can not judge whether the filaments are strings or sheets in edge-on configuration. Hester (1987) suggested that

thin sheet-like shock fronts are seen as filaments on the edge of the SNR. The filaments seen in figures of Hester (1987) resemble the structure in SN 1006. Furthermore, filaments should be also seen in the inner part of the shell if they are strings, however it is not the observed case. Therefore, we assume that the filaments have sheet-like structure normal to the shock direction. The depth of the sheet is unclear but would be similar to or smaller than the length of the filament. We thus assume the depth of the sheet to be about 1 pc in the following discussion.

The most likely scenario of cosmic ray acceleration at the SNR shock is diffusive shock acceleration (DSA). The predicted results from this model however are highly dependent on many parameters of the magnetic field, such as the angle between the magnetic field and shock normal direction, magnetic field strength and its fluctuation. Here, we investigate the observed profiles based on a DSA model, and estimate the physical quantities such as diffusion coefficient, the direction of magnetic field, maximum energy of accelerated electrons, and the injection efficiency. Although a realistic condition may be more complex as is discussed by Ellison, Berezhko, & Baring (2000) and Berezhko et al. (2002), we at first apply a simplest DSA model that the back reaction of accelerated particles is neglected.

4.2.1. Diffusion coefficient in upstream

The scale widths in the upstream side are largely scattered in the range of 0.98–11 arcsec (Table 2). Since this large scatter would be due to the projected effect of possible sheet-like structure with wavy and/or curved shape, real widths should be smaller than the observed (projected) width. To be conservative, we however adopted the mean value of 4.3 arcsec, or 0.04 pc at 1.8 kpc distance in the following discussion.

We use the results of *srcut*, the fit of the wide band spectra from X-ray to radio band. The high energy roll-off ν_{rolloff} *srcut* is the consequent of either age-limit (acceleration dominant), synchrotron loss, or diffusive escape (see § A.1). The best-fit ν_{rolloff} at the filaments is $2.6_{-0.7}^{+0.7} \times 10^{17}$ Hz, which can be converted to $1.1_{-0.3}^{+0.3}$ keV. These are consistent with the *ASCA* result of $3.0_{-0.2}^{+0.1} \times 10^{17}$ Hz or $1.24_{-0.08}^{+0.04}$ keV by Dyer et al. (2001).

Since most of the non-thermal X-ray photons are observed in the downstream region, the synchrotron radiation is mainly due to the downstream region. Using the best-fit ν_{rolloff} , we constrain the maximum energy of electrons E_{max} and magnetic field in downstream B_{d} from the eq.(A6);

$$E_{\text{max}} B_{\text{d}}^{0.5} = 0.37_{-0.06}^{+0.04} \quad [\text{ergs G}^{0.5}]. \quad (2)$$

In the case of the strong shock, the magnetic field in downstream B_{d} can be related to that

in upstream B_u as

$$B_d = (\cos^2 \theta_u + r^2 \sin^2 \theta_u)^{\frac{1}{2}} B_u, \quad (3)$$

where r and θ_u are the compression ratio and the magnetic field angle to the shock normal direction in upstream.

The diffusion coefficients in upstream (K_u) is estimated from eq.(A9) ($u_u = u_s$) as following;

$$\begin{aligned} K_u &\simeq w_u^h \cdot u_u = \overline{w_u^h} \cdot u_s \\ &= 3.1 \times 10^{25} \text{ [cm}^2\text{s}^{-1}\text{]}, \end{aligned} \quad (4)$$

where the shock speed u_s is assumed to be 2600 km s^{-1} (Laming et al. 1996). The diffusion coefficient in upstream is given from Using eq.(A10), we can derive K_u for the electrons of E_{\max} as,

$$K_u = \frac{1}{3} \xi_u \left(\cos^2 \theta_u + \frac{\sin^2 \theta_u}{1 + \xi_u^2} \right) \frac{E_{\max}}{e B_u} c, \quad (5)$$

where $\xi_u (> 1)$ is the fluctuation of the magnetic field.

We can derive following equations from eq.(2), (3), (4), and (5), the maximum energy (E_{\max}) and magnetic field in upstream (B_u) are,

$$\begin{aligned} E_{\max} &= 37 \xi_u^{-\frac{1}{3}} \left(\cos^2 \theta_u + \frac{\sin^2 \theta_u}{1 + \xi_u^2} \right)^{-\frac{1}{3}} \\ &\quad \times (\cos^2 \theta_u + r^2 \sin^2 \theta_u)^{-\frac{1}{6}} \text{ [TeV]}, \end{aligned} \quad (6)$$

$$\begin{aligned} B_u &= 4.0 \times 10^{-5} \xi_u^{\frac{2}{3}} \left(\cos^2 \theta_u + \frac{\sin^2 \theta_u}{1 + \xi_u^2} \right)^{\frac{2}{3}} \\ &\quad \times (\cos^2 \theta_u + r^2 \sin^2 \theta_u)^{-\frac{1}{6}} \text{ [G]}. \end{aligned} \quad (7)$$

Since SN 1006 is a type Ia SN located at a high latitude of 460 pc above the Galactic plane ($l = 14.6$ at 1.8 kpc distance), the interstellar magnetic field would be smaller than the typical value in the Galactic plane of the order of $10 \mu\text{G}$. We therefore conservatively assume that $B_u = 10 \mu\text{G}$, which is slightly larger than the combined results of the X-ray and TeV Gamma-rays (Tanimori et al. 2001). Then eq.(7) becomes,

$$\xi_u^{\frac{2}{3}} \left(\cos^2 \theta_u + \frac{\sin^2 \theta_u}{1 + \xi_u^2} \right)^{\frac{2}{3}} (\cos^2 \theta_u + r^2 \sin^2 \theta_u)^{-\frac{1}{6}} = 0.25. \quad (8)$$

For the parallel magnetic field ($\theta_u = 0^\circ$), ξ_u becomes smaller than 1. This unrealistically small value of ξ_u conflicts to a usual DSA which assume a parallel magnetic field configuration.

An alternative scenario is oblique magnetic field to the shock normal in this region ($\theta_u > 0^\circ$). For simplicity, we neglect the back reaction of accelerated particle, then the compression ratio becomes 4 for strong shock limit. The allowed region of θ_u is given from the eq.(8) as;

$$\theta_u \geq 82^\circ. \quad (9)$$

Thus the magnetic field in upstream near the filaments is almost perpendicular.

Assuming $\theta_u = 90^\circ$, $r = 4$, and $B_u = 10 \mu\text{G}$, E_{max} is given from eq.(6),

$$\begin{aligned} E_{\text{max}} &= r^{-\frac{1}{2}} B_u^{-\frac{1}{2}} \cdot 0.23_{-0.04}^{+0.03} \text{ [TeV]} \\ &= 37_{-7}^{+4} \text{ [TeV]}. \end{aligned} \quad (10)$$

When particles are accelerated very efficiently, their back reactions to the shock can not be ignored hence r becomes larger than 4. Even if the compression ratio is the largest of $r = 7$ (Ellison, Berezhko, & Baring 2000; Berezhko et al. 2002), the allowed range is $\theta_u > 80^\circ$. Therefore, we can safely predict that the magnetic field in the NE shell of SN 1006 is nearly perpendicular to the shock normal.

As for the downstream region, the observed spatial profile seems to be incompatible with the solution derived by Blandford & Ostriker (1978). The maximum electron energy E_{max} would be determined by the balance of the time scales between the accelerating and the synchrotron cooling. These time scales may depend on the structure and the fluctuation of the magnetic field along the shock normal; both time scales become smaller with larger magnetic field, while the former becomes also smaller with larger fluctuation of the magnetic field.

The shock flow may compresses and partly stretches the magnetic field in the radial direction, which may produce highly disordered magnetic field with small fraction of radial component, as discussed by Reynolds & Gilmore (1993) with the radio polarization data, who reported that only 15–20% of the magnetic-field energy in SN 1006 NE shell in radial polarization, and most of the magnetic field is disordered with the scale smaller than 0.2 pc.

To determine the magnetic field in downstream, we thus need require more complicated processes such as the history of the shock propagation and the non-linear effect, and many assumptions, which is beyond this paper and would leave for a future study.

4.2.2. Injection Efficiency

We define the injection efficiency $\eta \equiv \frac{n_e^{\text{NT}}}{n_e^{\text{T}}}$, where n_e^{NT} and n_e^{T} are the number densities of non-thermal and thermal electrons in the filaments. The depth of the filament (sheet-like) is assumed to be 1 pc (see § 4.2.1), with uniform electron density.

The non-thermal electron flux (energy) are estimated using the method given in Appendix (§ A.1), where the non-thermal X-ray flux and spectra of each filament are taken from Table 2 and Table 3. We adopt the minimum energy of non-thermal electrons (injection energy) E_{min} to be 0.24 keV (the temperature of the thermal plasma; see Table 1). The magnetic field and the maximum energy are unknown parameters, however we can suggest that the magnetic field in downstream is significantly larger than that in upstream. In this section, we adopt the magnetic field B to be perpendicular to the shock normal, $B_d = 4B_u = 40 \mu\text{G}$ arbitrary and the maximum energy E_{max} to be 37 TeV from the discussion in § 4.2.1. The derived number density (n_e^{NT}), the total number (N_e^{NT}), and the total energy (E_e^{NT}) of non-thermal electrons in each filament are summarized in Table 4.

For the estimation of thermal electron flux (energy), we adopted the projected profile of the thermal X-rays (the soft2 band) given in Table 2 and the spectral parameters of thermal plasma given in Table 3. The resultant number density (n_e^{T}), total number (N_e^{T}), and total energy (E_e^{T}) of thermal electrons in each filament are given in Table 4. The injection efficiency η ($\equiv \frac{n_e^{\text{NT}}}{n_e^{\text{T}}}$) is then obtained as is shown in Table 4. All the values η are nearly identical in each filament of $\sim 1 \times 10^{-3}$ but are about 2 times larger than 5×10^{-4} derived from the *ASCA* data by Allen, Petre, & Gotthelf (2001), although they also assumed as $B_d = 40 \mu\text{G}$ arbitrary. For comparison, we estimate η with larger magnetic field of $B_d = 40 \mu\text{G}$, and find a larger η than Allen, Petre, & Gotthelf (2001). They estimated the number density of non-thermal electrons from larger regions than the filaments, because *ASCA* could not resolve the filaments. On the other hand, we found that the non-thermal electrons are confined in the thin filaments, which are the sites of ongoing acceleration of the non-thermal electrons. We thus regard that the present *Chandra* result suggests that the injection occurs more locally and more efficiently and as a result, it must be more realistic estimation of η than that by Allen, Petre, & Gotthelf (2001).

The energy densities of the magnetic field, the thermal plasma, and the non-thermal electrons in the filaments are $6.4 \times 10^{-11} \text{ ergs cm}^{-3}$, $2.6 \times 10^{-10} \text{ ergs cm}^{-3}$, and $6.9 \times 10^{-11} \text{ ergs cm}^{-3}$, respectively. Thus, at the shocked region, the magnetic field and non-thermal electrons are in energy equi-partition and are slightly smaller than the thermal energy (about 30%).

As suggested by Ellison, Berezhko, & Baring (2000), the non-thermal protons should

carry larger energy than electrons, hence particle energy becomes larger than that of magnetic and possibly that of thermal. We therefore must consider non-linear effects suggested by Ellison, Berezhko, & Baring (2000) and by Berezhko et al. (2002), however more quantitative scenario including the non-linear effects must be a future work.

5. Summary

(1) X-ray emissions from the NE shell of SN 1006 are found to be composites of filaments, clumps and more extended diffuse emissions. We resolved the thermal and non-thermal X-rays using the different spectral shape and morphology.

(2) The spectrum of the thermal component has $kT = 0.24$ keV temperature and relatively small ionization time scale $n_e\tau = 1.1 \times 10^{10}$ s cm⁻³. The chemical compositions are overabundant, especially in iron, which suggests that the X-ray emitting plasma originates from ejecta and the progenitor is type Ia.

(3) The non-thermal components can be described with a power-law function with the photon index 2.1–2.3 in the narrow filaments and 2.5 at the inner region of the shell.

(4) The structure of the filaments shows different characteristics in thermal and non-thermal X-rays. The thermal plasma has the scale width of 1 pc in downstream, similar to the shock width derived from Sedov equations. The non-thermal filaments show extremely small scale width of $w_u^h \sim 0.04$ pc and $w_d^h \sim 0.2$ pc, in upstream and downstream, respectively.

(5) In a diffusive shock acceleration model, the observed thin filaments requires a nearly perpendicular magnetic field with the angle between the magnetic field in upstream (assumed as 10 μ G) and the shock normal of larger than $\sim 80^\circ$. The maximum energy of the electrons are 30–40 TeV.

(6) The injection efficiency is estimated to be $\eta = 1 \times 10^{-3}$, suggesting that thermal particles are injected locally and very effectively. Then the energy density of non-thermal electrons becomes comparable to that of the magnetic field and about 30% of the thermal energy density. Thus non-linear effect of the shock structure and acceleration mechanism must be considered.

We thank the anonymous referee for his/her helpful comments. Our particular thanks are due to M. Hoshino, T. Terasawa, T. Yoshida, and S. Inutsuka for their fruitful discussions and comments. A.B. and M.U. are supported by JSPS Research Fellowship for Young Scientists.

A. Appendix

In this appendix, we briefly introduce the relevant software tools and equations, which are used for the discussions in the text.

A.1. Electron Spectra and *srcut* Model

The spectrum of non-thermal electrons accelerated by the diffusive shock is (Bell 1978);

$$\frac{dn_e^{\text{NT}}}{dE^{\text{NT}}} = \kappa(E^{\text{NT}} + m_e c^2)(E^{\text{NT}2} + 2m_e c^2 E^{\text{NT}})^{-\frac{(p+1)}{2}} \times \exp(-E^{\text{NT}}/E_{\text{max}}), \quad (\text{A1})$$

where n_e^{NT} and E^{NT} are the number density and the energy of non-thermal electrons, respectively.

The synchrotron radiation power per unit frequency from a single electron of energy E in a magnetic field B is

$$P(\nu, \alpha) = \frac{\sqrt{3}e^3 B \sin \alpha}{m_e c^2} F\left(\frac{\nu}{\nu_c}\right), \quad (\text{A2})$$

where α and $F(x)$ are the pitch angle and the function given by Rybicki & Lightman (1979). The peak frequency ν_c is

$$\nu_c = \frac{3cE^2 e B \sin \alpha}{4\pi(m_e c^2)^3}. \quad (\text{A3})$$

Convolving the eq.(A1) with (A2), we obtain the spectrum of synchrotron radiation in the pitch angle α as,

$$f(\nu, \alpha) = \int_{E_{\text{min}}}^{\infty} dE^{\text{NT}} \frac{dn_e^{\text{NT}}}{dE_e^{\text{NT}}} P(\nu, \alpha). \quad (\text{A4})$$

Averaged over the pitch angle, we finally obtain the synchrotron radiation energy per unit volume, frequency, and time,

$$f(\nu) = \frac{1}{2} \int_0^\pi d\alpha \sin \alpha f(\nu, \alpha). \quad (\text{A5})$$

The observed spectrum is fitted with this model spectrum using the *Chandra* software *srcut* with 3 free parameters (Reynolds 1998; Reynolds & Keohane 1999). The normalization constant and spectral index are determined so as to reproduce the flux and slope in the radio band. These parameters are converted to κ and p in eq.(A1). The other fitting parameter ν_{rolloff} is a function of E_{max} in eq.(A1) and magnetic field (B) as is shown below (Reynolds & Keohane 1999);

$$\nu_{\text{rolloff}} = 0.5 \times 10^{16} \left(\frac{B}{10 \mu\text{G}} \right) \left(\frac{E_{\text{max}}}{10 \text{ TeV}} \right)^2 \quad [\text{Hz}]. \quad (\text{A6})$$

This equation gives constraint on the maximum electron energy E_{max} and magnetic field B .

Since available radio data of SN 1006 have spatial resolution far larger than the scale of the X-ray filaments, we have no accurate radio flux nor index from the position of the X-ray filaments. We therefore fixed the radio index to the poor resolution radio result of $p = 2.14$ by Allen, Petre, & Gotthelf (2001) and the radio flux is treated as a free parameter for the present *srcut* fitting. Allowing the radio index to vary from $p = 2.0$ to $p = 2.2$, we see no significant difference in the best-fit parameters within the statistical errors.

A.2. Diffusion versus Advection

The spatial structure of the relativistic electrons produced by the diffusive shock acceleration across the shock is determined by the competing process of diffusion and advection. The advection time scale (τ_{ad}) is given by

$$\tau_{\text{ad}} = \frac{w}{u}, \quad (\text{A7})$$

where w is the scale width of the spatial distribution of the relativistic electrons and u is the flow speed.

The diffusion time scale (τ_{dif}) is given from the random-walk theory as;

$$\tau_{\text{dif}} = \frac{w^2}{K}, \quad (\text{A8})$$

where K is the diffusion coefficient.

In order that the high energy electrons are accelerated at shock front, electrons in upstream should be diffused back to the shock front against the advection to the downstream side (shock flow). Therefore, τ_{ad} should be nearly equal to τ_{dif} , hence $\frac{w_{\text{u}}}{u_{\text{u}}} \simeq \frac{w_{\text{u}}^2}{K_{\text{u}}}$. We thus obtain;

$$w_{\text{u}} \simeq \frac{K_{\text{u}}}{u_{\text{u}}}. \quad (\text{A9})$$

For more exact formalisms, see e.g. Bell (1978), Blandford & Ostriker (1978), and Drury (1983).

Let the mean free path parallel to the magnetic field be a constant factor ξ times the gyro radius r_{g} . Then, the effective diffusion coefficient along the shock normal is given as

(Jokipii 1987; Skilling 1975)

$$K = \frac{1}{3}\xi r_g c \left(\cos^2 \theta_u + \frac{\sin^2 \theta_u}{1 + \xi^2} \right), \quad (\text{A10})$$

$$r_g = \frac{E_e}{eB}, \quad (\text{A11})$$

where e , E_e , B , and θ_u are the electric charge, the energy of relativistic electrons, and the magnetic field, and the angle between the magnetic field in upstream and the shock normal, respectively.

REFERENCES

- Aharonian, F.A., & Atoyan, A.M. 1999, *A&A*, 351, 330
- Allen, G.E., Petre, R., & Gotthelf, E.V. 2001, *ApJ*, 558, 739
- Anders, E., & Grevesse, N. 1989, *Geochim. Cosmochim. Acta*, 53, 197
- Bamba, A., Tomida, H., & Koyama, K. 2000, *PASJ*, 52, 1157
- Bell, A.R. 1978, *MNRAS*, 182, 443
- Berezhko, E.G., Ksenofontov, L.T. Völk, H.J. 2002, *astro-ph/0204085*
- Blandford, R.D., & Eichler, D. 1987, *Phys. Rep.*, 154,1
- Blandford, R.D., & Ostriker, J.P. 1978, *ApJ*, 221, L29
- Borkowski, K.J., Lyerly, W.J., & Reynolds, S.P. 2001a, *ApJ*, 548, 820
- Borkowski, K.J., Rho, J., Reynolds, S.P. & Dyer, K.K. 2001b, *ApJ*, 550, 334
- Drury, L.O’C. 1983, *Rep. Prog. Phys.*, 46, 973
- Dyer, K.K., Reynolds, S.P., Borkowski, K.J., Allen, G.E., & Petre, R. 2001, *ApJ*, 551, 439
- Ellison, D.C., Berezhko, E.G., & Baring, M.G. 2000, *ApJ*, 540, 292
- Enomoto, R., Tanimori, T., Naito, T., Yoshida, T., Yanagita, S., Mori, M., Edwards, P.G., Asahara, A. et al. 2002, *Nature*, 416, 823
- Garmire, G., Feigelson, E.D., Broos, P., Hillenbrand, L.A., Pravdo, S.H., Townsley, L., & Tsuboi, Y. 2000, *AJ*, 120, 1426

- Green, D.A. 2001, A Catalogue of Galactic Supernova Remnants (2001 December version), (Cambridge, UK, Mullard Radio Astronomy Observatory) available on the WWW at <http://www.mrao.cam.ac.uk/surveys/snrs/>
- Hess, V.F. 1912, *Phys. Zeits.*, 13, 1084
- Hester, J.J. 1987, *ApJ*, 314, 187
- Jokipii, J.R. 1987, *ApJ*, 313, 842
- Jones, F.C., & Ellison, D.C. 1991, *Space Science Rev.*, 58, 259
- Koyama, K., Petre, R., Gotthelf, E.V., Hwang, U., Matura, M., Ozaki, M., & Holt S.S. 1995, *Nature*, 378, 255
- Koyama, K., Kinugasa, K., Matsuzaki, K., Nishiuchi, M., Sugizaki, M., Torii, K., Yamauchi, S., & Aschenbach, B. 1997, *PASJ*, 49, L7
- Laming, J. M., Raymond, J. C., McLaughlin, B. M., & Blair, W. P. 1996, *ApJ*, 472, 267
- Malkov, E., & Drury, L.O’C. 2001, *Rep. Prog. Phys.*, 64, 429
- Morrison, R., & McCammon, D. 1983, *ApJ*, 270, 119
- Muraishi, H., Tanimori, T., Yanagita, S., Yoshida, T., Moriya, M., Kifune, T., Dazeley, S.A., Edwards, P.G. et al. 2000, *A&A*, 354, L57
- Reynolds, S.P., & Gilmore, D.M. 1993, 106, 272
- Reynolds, S.P. 1998, *ApJ*, 493, 375
- Reynolds, S.P., & Keohane, J.W. 1999, *ApJ*, 525, 368
- Rybicki, G.B., & Lightman, A.P. 1979, “Radiative Processes in Astrophysics”, Wiley-Interscience, New York
- Skilling, J. 1975, *MNRAS*, 172, 557
- Slane, P., Gaensler, B.M., Dame, T.M., Hughes, J.P., Plucinsky, P.P., & Green, A. 1999, *ApJ*, 525, 357
- Slane, P., Hughes, J.P., Edgar, R.J., Plucinsky, P.P., Miyata, E., Tsunemi, H., Aschenbach, B. 2001, 548, 814

Tanimori, T., Hayami, Y., Kamei, S., Dazeley, S.A., Edwards, P.G., Gunji, S., Hara, S., Hara, T. et al. 1998, *ApJ*, 497, L25

Tanimori, T., Naito, T., Yoshida, T., & CANGAROO collaboration 2001, to appear in proceedings of 27th ICRC, astro-ph/0108031

Vink, J., Kaastra, J.S., Bleeker, J.A.M., & Preite-Martinez, A. 2000, *A&A Rev.*, 354, 931

Weisskopf, M.C., O'dell, S.L., & van Speybroeck, L.P. 1996, *Proc. SPIE*, 2805, 2

Winkler, P.F. & Long, K.S. 1997, *ApJ*, 491, 829



Fig. 1.— The true-color images of SN 1006 NE shell binned with 1 arcsec scale. Red and blue are 0.5-2.0 keV and 2.0-10.0 keV, respectively, both in logarithmic scale.

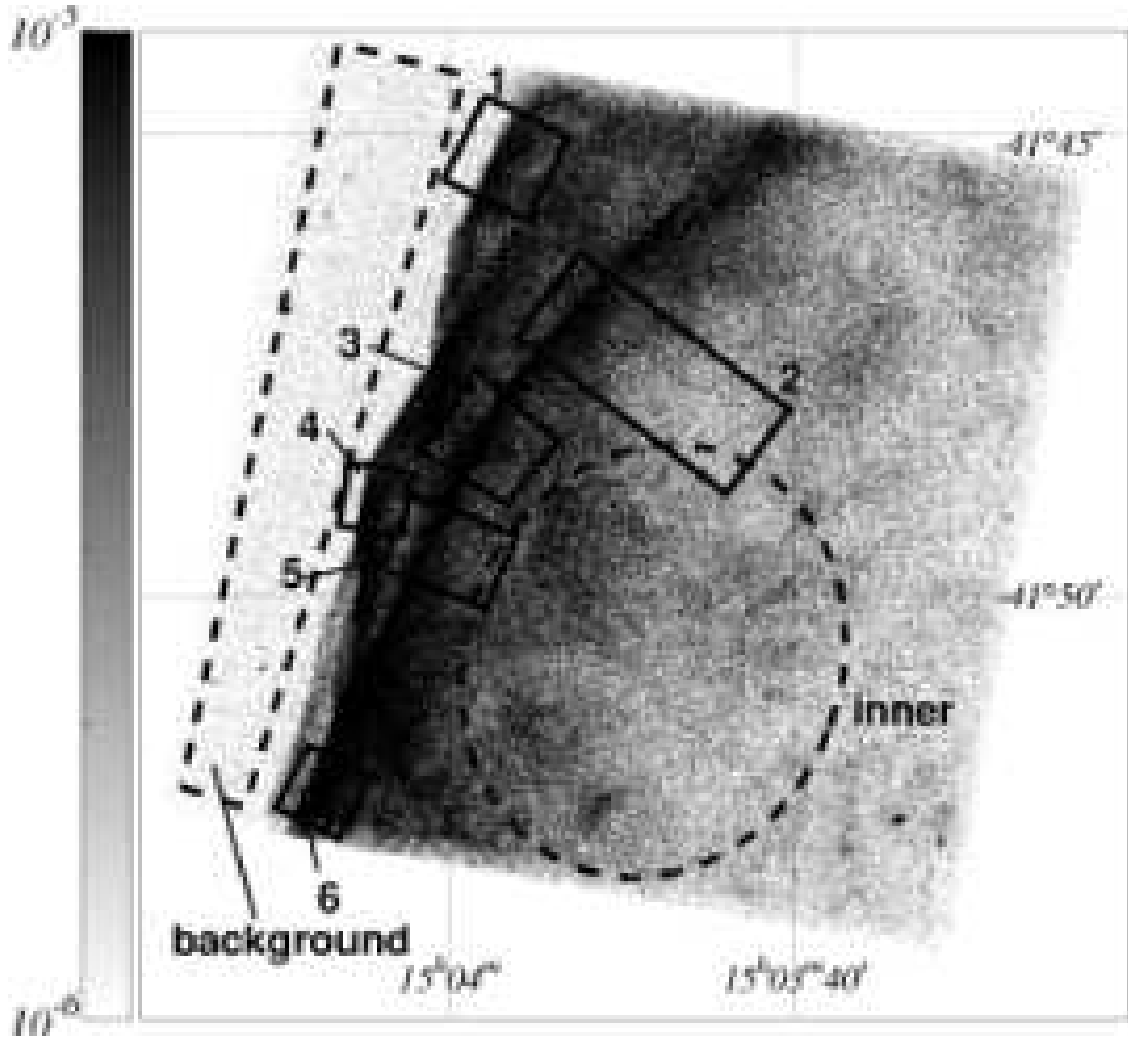


Fig. 2.— The close-up view of the 0.5–10.0 keV band image of S3 chip with J2000 coordinates, binned with 1 arcsec scale. The gray scale (the left bar) is given logarithmically ranging from 1×10^{-6} to 1×10^{-5} cts s⁻¹ arcsec⁻². The inner and background regions for the spectral analyses and the filament regions for the spatial analyses (No.1–6) are shown with dashed and solid lines, respectively.

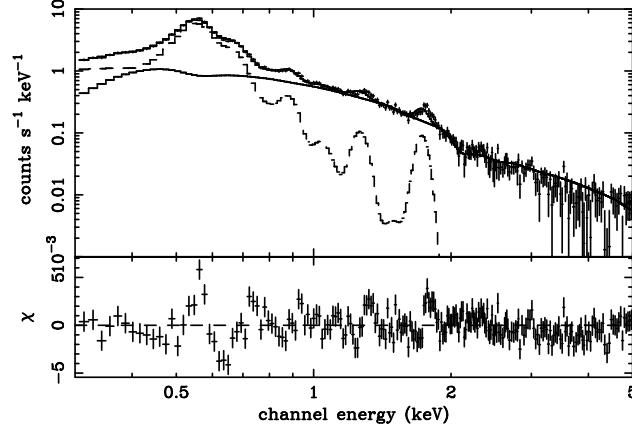


Fig. 3.— The upper panel: The background-subtracted spectrum of the inner region (crosses). Dashed line and solid lines are the best-fit thin thermal and power-law models, respectively. The lower panel: The data residuals from the best-fit two-components model.

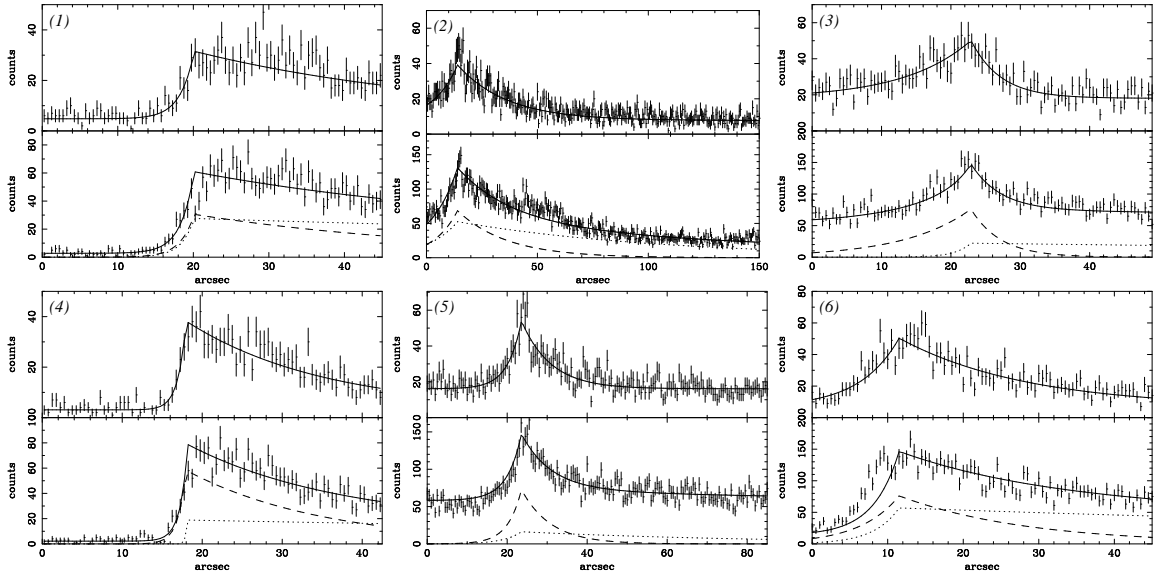


Fig. 4.— The profiles of the filaments in SN 1006 NE shell. Upper panels show the profiles in the hard (2.0–10.0 keV) band, whereas the lower panels in the soft2 (0.4–0.8 keV) band with the best-fit models (solid lines). The dashed lines in the lower panels represent non-thermal photons extrapolated from the hard band flux of the power-law (see the upper panels). The dotted lines are the thermal component after subtracting the non-thermal contamination (dashed lines). Upstream is to the left and downstream is to the right.

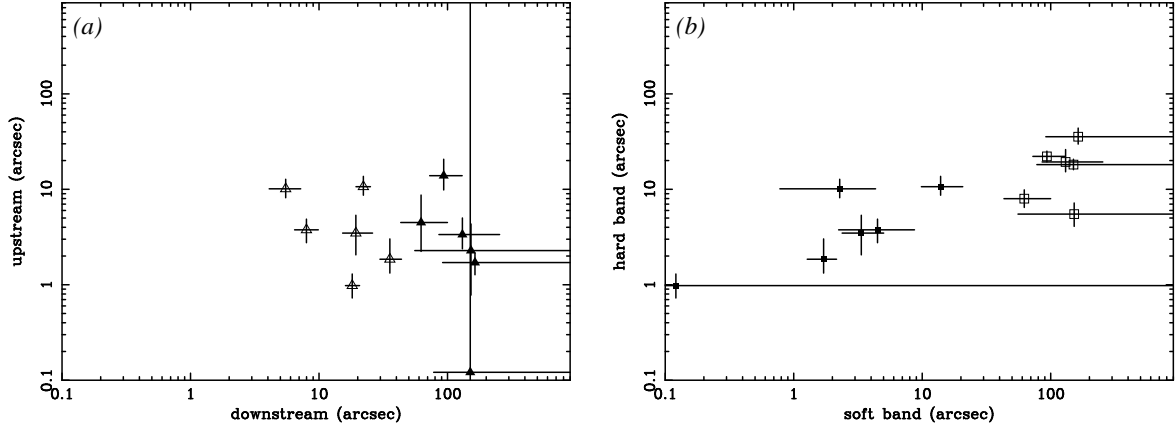


Fig. 5.— (a) The relation between w_u and w_d . The close and open triangles are for the thermal and non-thermal emissions, respectively. (b) The relation between w^s and w^h . The close and open boxes are in the upstream and downstream, respectively.

Table 1. The best-fit parameters of the spectrum of the inner region^a

Parameters	Best-fit value
Power-law Model	
Photon Index	2.51 (2.48–2.53)
Flux ^b [ergs cm ⁻² s ⁻¹] . . .	3.8×10^{-12}
NEI model	
Temperature [keV]	0.24 (0.21–0.26)
Abundances ^c	
C	(<0.1)
N	(<0.03)
O	3.3 (3.0–3.5)
Ne	4.8 (4.4–5.2)
Mg	51 (42–61)
Si	131 (121–140)
S	10 (6.8–13)
Fe	37 (28–46)
$n\tau$ [$\times 10^9$ s cm ⁻³]	10.8 (9.9–11.1)
$E.M.$ ^d [$\times 10^{55}$ cm ⁻³]	2.1 (1.9–2.2)
Flux ^b [ergs cm ⁻² s ⁻¹] . . .	3.3×10^{-12}
N_H [10^{20} H cm ⁻²]	9.0 (8.5–9.4)
Reduced χ^2 [χ^2 /d.o.f]	447.9/215

^aParentheses indicate single-parameter 90% confidence regions.

^bIn the 0.3–10.0 keV band.

^cAbundance ratio relative to the solar value (Anders & Grevesse 1989).

^d $E.M. = n_e^2 V$, where n_e and V are the electron density and the volume, respectively.

Table 2. The best-fit parameters of the profiles of the filaments.^a

No.	A^h [cnts arcsec ⁻¹] ^b	w_u^h [arcsec]	w_d^h [arcsec]	Reduced χ^2 [χ^2 /d.o.f.]	A^s [cnts arcsec ⁻¹] ^c	w_u^s [arcsec]	w_d^s [arcsec]	Reduced χ^2 [χ^2 /d.o.f.]
1 ...	53 (49–58)	1.9 (1.3–3.0)	36 (30–44)	119.1/105 ...	55 (49–61)	1.7 (1.3–2.2)	1.6×10^2 (>92)	104.0/94 ...
2 ...	63 (58–68)	11 (8.7–14)	22 (19–25)	347.3/296 ...	1.0×10^2 (95– 1.2×10^2)	14 (9.8–21)	93 (73– 1.3×10^2)	481.8/298 ...
3 ...	66 (58–74)	10 (8.2–13)	5.5 (4.1–7.2)	141.3/114 ...	44 (37–52)	2.3 (0.78–4.3)	1.5×10^2 (>56)	119.8/95 ...
4 ...	68 (62–74)	0.98 (0.73–1.3)	18 (16–21)	103.2/99 ...	38 (34–42)	0.12 (not determined)	1.5×10^2 (>78)	106.1/81 ...
5 ...	75 (66–85)	3.8 (2.8–4.9)	8.0 (6.5–9.9)	218.3/166 ...	33 (24–41)	4.5 (2.2–8.7)	62 (43– 1.0×10^2)	236.5/167 ...
6 ...	87 (79–96)	3.5 (2.1–5.4)	19 (15–26)	99.9/86 ...	1.1×10^2 (1.0×10^2 – 1.3×10^2)	3.4 (2.4–5.0)	1.3×10^2 (86– 2.5×10^2)	118.4/87 ...

^aParentheses indicate single-parameter 90% confidence regions.

^bIn the 2.0–10.0 keV band.

^cIn the 0.4–0.8 keV band.

Table 3. The best-fit parameters of the spectral fittings for the filaments.^a

Parameters	1	2	3	4	5	6	Total
Power-low model							
Γ	2.0 (1.8–2.2)	2.4 (2.3–2.6)	2.3 (2.1–2.4)	2.3 (2.1–2.4)	2.3 (2.1–2.5)	2.3 (2.1–2.4)	2.31 (2.29–2.33)
N_H [10^{21} H cm ⁻²]	1.5 (0.9–2.1)	1.8 (1.5–2.0)	1.2 (1.0–1.5)	1.6 (1.3–2.0)	1.4 (1.1–1.8)	1.4 (1.1–1.7)	1.6 (1.6–1.7)
Flux ^b [ergs cm ⁻² s ⁻¹] ..	3.7×10^{-13}	5.4×10^{-13}	3.7×10^{-13}	2.5×10^{-13}	2.3×10^{-13}	4.2×10^{-13}	1.8×10^{-12}
Reduced χ^2 [χ^2 /d.o.f.] .	44.1/43	232.5/164	196.3/140	139.8/125	143.8/125	173.4/130	273.3/211
<i>srcut</i> model							
ν_{rolloff} [$\times 10^{17}$ Hz]	13 (3.6–94)	1.7 (1.1–2.3)	2.8 (1.8–4.7)	2.9 (1.5–6.2)	2.4 (1.3–5.0)	2.8 (1.7–5.0)	2.6 (1.9–3.3)
N_H [10^{21} H cm ⁻²]	1.3 (1.0–1.7)	1.4 (1.2–1.5)	1.0 (0.8–1.1)	1.3 (1.1–1.5)	1.1 (0.9–1.4)	1.1 (0.9–1.3)	1.3 (1.2–1.5)
Flux ^b [ergs cm ⁻² s ⁻¹] ..	3.6×10^{-13}	5.3×10^{-13}	3.6×10^{-13}	2.4×10^{-13}	2.2×10^{-13}	4.1×10^{-13}	1.8×10^{-12}
Reduced χ^2 [χ^2 /d.o.f.] .	43.7/43	225.1/164	190.9/140	139.1/125	141.1/125	170.7/130	265.2/211

^aParentheses indicate single-parameter 90% confidence regions.

^bIn the 0.3–10.0 keV band.

Table 4. The number densities and energies of thermal and non-thermal electrons

Filament No.	1	2	3	4	5	6	Total
Thermal electrons							
EM [cm^{-3}].....	7.0×10^{53}	1.0×10^{54}	1.3×10^{53}	2.5×10^{53}	1.3×10^{53}	8.4×10^{53}	3.1×10^{54}
Density (n_e^T) ^a [cm^{-3}]....	0.43	0.51	0.26	0.41	0.30	0.60	0.45
Total number (N_e^T).....	1.6×10^{54}	2.1×10^{54}	5.0×10^{53}	6.1×10^{53}	4.3×10^{53}	1.4×10^{54}	6.8×10^{54}
Energy (E_e^T) ^b [ergs].....	9.2×10^{44}	1.2×10^{45}	2.8×10^{44}	3.5×10^{44}	2.4×10^{44}	7.9×10^{44}	3.9×10^{45}
Non-thermal electrons ^c							
Density (n_e^{NT}) ^a [cm^{-3}]...	4.7×10^{-4}	5.5×10^{-4}	7.9×10^{-4}	7.1×10^{-4}	6.5×10^{-4}	7.6×10^{-4}	6.2×10^{-4}
Total number (N_e^{NT})....	1.8×10^{51}	2.2×10^{51}	1.5×10^{51}	1.1×10^{51}	9.4×10^{50}	1.8×10^{51}	9.3×10^{51}
Energy (E_e^{NT}) [ergs]....	2.0×10^{44}	2.4×10^{44}	1.7×10^{44}	1.2×10^{44}	1.1×10^{44}	2.0×10^{44}	1.0×10^{45}
Injection efficiency (η) ^d	1.1×10^{-3}	1.1×10^{-3}	3.0×10^{-3}	1.7×10^{-3}	2.2×10^{-3}	1.3×10^{-3}	1.4×10^{-3}

^aWe assumed that the depth of the emitting volume is 1 pc and that the filling factor = 1.

^b $E_e^T = \frac{3}{2}n_e V^{NT} kT$.

^cIntegration from $E_{\min} = 0.24$ keV to $E_{\max} = 37$ TeV (see text).

^d $\eta \equiv \frac{n_e^{NT}}{n_e^T}$ (see text).